Open Journal of Civil Engineering, 2025, 15(4), 797-812
https://www.scirp.org/journal/ojce
ISSN Online: 2164-3172
ISSN Print: 2164-3164

Image Analysis-Based Study on Influencing Factors and Reliability in Soil Dynamic Deformation Time-History Identification

Jingjing Ding[1,2]**, Xuefeng Duan**[1*]

[1]Yanzhao Modern Transportation Laboratory, Shijiazhuang Tiedao University, Shijiazhuang, China
[2]School of Environmental and Municipal Engineering, North China University of Water Resources and Electric Power, Zhengzhou, China
Email: *dxf@stdu.edu.cn

How to cite this paper: Ding, J.J. and Duan, X.F. (2025) Image Analysis-Based Study on Influencing Factors and Reliability in Soil Dynamic Deformation Time-History Identification. *Open Journal of Civil Engineering*, **15**, 797-812.
https://doi.org/10.4236/ojce.2025.154044

Received: September 26, 2025
Accepted: December 9, 2025
Published: December 12, 2025

Abstract

Image deformation analysis techniques are widely used in geotechnical engineering. However, research on identifying the time history of dynamic soil deformation remains limited, and the reliance on empirical parameter selection often leads to unstable identification accuracy. To evaluate the applicability of these techniques for dynamic deformation time-history identification and to determine the key influencing factors, this study employs both the Reliability-guided digital image correlation and PIVlab methods on digitally simulated images of sandy soil. It systematically analyzes the effects of strain calculation window size, image acquisition frame rate, and deformation magnitude on the identification accuracy of displacement, acceleration, and strain time histories. The reliability of these techniques is also validated. The results indicate that under constant strain conditions, the calculation error decreases with an increase in the predefined strain value. Accordingly, the required minimum window sizes are no less than 17 × 17, 13 × 13, and 5 × 5 for strain levels of 0.1%, 1%, and 10%, respectively. Under sinusoidal loading, a frame rate equal to or exceeding six times the loading frequency can limit the displacement and acceleration errors to within 10% and 20%, respectively. For specific seismic waveforms—Northridge, Loma Gilroy, and Tangshan—the minimum frame rates required are 20 Hz, 10 Hz, and 6 Hz, respectively. When the deformation amplitude is ≥0.1 mm, the errors associated with both methods are comparable. However, for amplitudes ≤ 0.01 mm, PIVlab demonstrates superior accuracy in displacement identification. Notably, under large deformation conditions, PIVlab is prone to accumulating outliers, and its errors are significantly amplified upon differentiation to obtain acceleration. This study establishes key parameter thresholds and elucidates the technical characteristics of different methods, providing valuable references and guidance for soil dynamics experiments and the engineering measurement of dynamic deformations.

Keywords

Image Deformation Analysis, DIC, Dynamic Soil Deformation, Parameter Optimization

1. Introduction

Deformation constitutes one of the most critical challenges in geotechnical earthquake engineering, with numerous instances of seismic damage and the substantial losses incurred being primarily attributable to deformation. Image-based deformation measurement techniques enable non-contact, non-intrusive, and full-field monitoring of soil deformation [1]-[4]. These methods facilitate the acquisition of deformation status at any point on the observed surface at any given time, thereby effectively capturing key information regarding the progression of soil failure. As such, they complement traditional sensor-based measurement approaches and represent a powerful tool for obtaining deformation data in geotechnical contexts.

Image deformation measurement technologies are widely employed in geotechnical engineering and have proven highly effective in generating displacement vector fields and contour maps of measurement surfaces [5]-[8]. However, existing applications are predominantly confined to static deformation measurements or to capturing specific states during dynamic events (e.g., before and after vibration loading). The stress-strain relationship of soils, along with their evolutionary development prior to failure and their instantaneous state at failure, is crucial for analyzing dynamic soil properties, failure mechanisms, and threshold conditions [9]-[11]. Consequently, the capability to observe the dynamic response at any point within the soil mass and to monitor the failure process during vibration is key to advancing the application of image-based techniques in soil dynamics analysis.

Dynamic deformation measurement presents greater complexity compared to static observation: 1) The measured object vibrates relative to the image acquisition equipment, necessitating consideration of this relative motion, which is typically addressed by installing reference points inside the model container [1] [12]. 2) A sufficiently high sampling frequency and analytical precision are required to track the dynamic response process. This demands camera equipment with a high enough frame rate to capture the entire process, particularly given the significant time scaling factors (ranging from tens to hundreds) involved in centrifuge model tests [13]-[15]. 3) The immense volume of data generated requires analytical parameters to be adjusted automatically and adaptively based on the deformation.

Key parameter adjustments include the subset size for displacement analysis and the window size for strain calculation [16]-[19]. Currently, these parameters are often determined empirically through iterative trial calculations, an approach that yields unstable and unreliable results and is highly impractical for the large datasets characteristic of dynamic measurements.

Addressing these challenges, this study leverages the advantage of soil image simulation technology, which allows for the preset of deformation patterns and magnitudes as required. It evaluates the feasibility and performance of image-based deformation measurement techniques in extracting displacement and acceleration time histories under varying dynamic load frequencies and image acquisition frame rates, as well as in strain calculation under different window sizes and deformation conditions. The findings aim to provide guidance and a valuable reference for subsequent research and for practical application in physical experiments and engineering tests.

2. Soil Simulation Image and Preset Deformation Time History

The soil images and dynamic deformation sequences were generated using the sand image simulation method proposed by Wang Yongzhi *et al.* [20]. This method is specifically designed for the calibration of soil deformation measurement techniques and provides notable advantages over the Gaussian speckle method: it not only closely replicates the soil's structural, morphological, and color characteristics but also precisely simulates the deformation process based on a predefined deformation field. Moreover, by adjusting the generation parameters, the method enables systematic analysis of the effects of image parameters, observational conditions, lens distortion, particle shape and size, texture characteristics, and porosity on the performance of image measurement techniques.

In this study, fundamental parameters of Fujian standard sand—including d_{50}, roundness, and color distribution—were employed. With an observational area of 304 mm × 192 mm, simulated images at a resolution of 3800 pixels × 2400 pixels were generated. For image deformation analysis, the internationally widely-used Reliability-guided digital image correlation (RG-DIC) method was selected. The widely accepted and used international methods for measuring image deformation are RG-DIC and PIVlab [11] [21].

2.1. One-Dimensional Translational Dynamic Time History

The one-dimensional translational dynamic time histories were simulated using sinusoidal waves of various frequencies and real ground motion records (including the Northridge, Loma Gilroy, and Tangshan waves) as input loads. This was done to determine the suitable image acquisition frame rates required for the image deformation measurement technique to accurately capture displacement and acceleration time histories under these different excitations. The Northridge, Loma Gilroy, and Tangshan waves are primarily characterized by high, medium, and medium-to-low frequency components, respectively. Together, they encompass a broad frequency spectrum, thus facilitating the investigation into the effects of load characteristics and frequency content on the performance of the image-based technique in measuring dynamic soil displacement and acceleration time histories.

2.2. Dynamic Time History of Translation and Shear Superposition

The dynamic time history combining translation and shear was simulated through superposition of translational motion and shear deformation formulations. Let $\left(x_0^n, y_0^n\right)$ denote the initial coordinates of the *n*-th particle in the image, where $n = 1, \cdots, N$; and let $\left(x_t^n, y_t^n\right)$ represent the position of the *n*-th particle at time *t*. The dynamic translation functions along the orthogonal *x*- and *y*-directions are defined as $u(t)$ and $v(t)$, respectively. Each particle is assumed to be located at the deformation center of a soil unit with length ΔL and height Δh Denote the horizontal motion function of the soil unit as $p\left(t, y_0^n\right)$ and the shear strain function as $\gamma\left(t, y_0^n\right)$.The total horizontal displacement is then given by: $\gamma\left(t, y_0^n\right)\frac{\Delta h}{2} + p\left(x_0^n, y_0^n\right) + u(t)$, This expression accounts for both the horizontal movement of the soil unit and the relative motion of the particle within the unit. Thus, the position of each particle at time *t* can be described as follows:

$$\begin{bmatrix} x_t^n \\ y_t^n \end{bmatrix} = \begin{bmatrix} 1 & 0 & \gamma\left(t, y_0^n\right)\frac{\Delta h}{2} + p\left(x_0^n, y_0^n\right) + u(t) \\ 0 & 1 & v(t) \end{bmatrix} \begin{bmatrix} x_0^n \\ y_0^n \\ 1 \end{bmatrix} \tag{1}$$

A simulated image of artificial sand, generated using Equation (1) to represent combined translation and uniform shear, is shown in **Figure 1**. The figure clearly demonstrates the deformation effects under superimposed translational and shear loading, illustrating the overall morphologic evolution of the sand subjected to this composite motion.

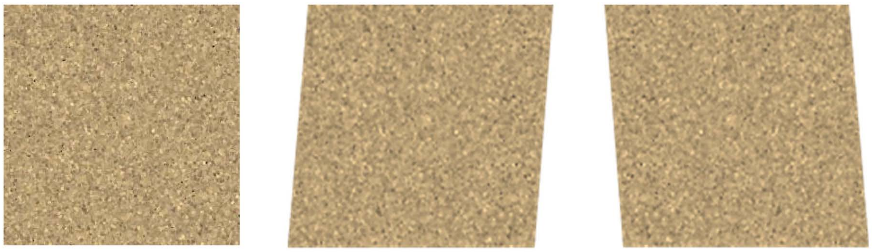

Figure 1. Simulation image of uniform shear deformation of sand.

2.3. Non-Uniform Shear Deformation Time History

The realization of non-uniform shear deformation artificial sand simulation image is defined by trigonometric function, as shown in Equation (2). The simulated images of artificial sand generated by translation and shear superposition according to Equation (2) are shown in **Figure 2**.

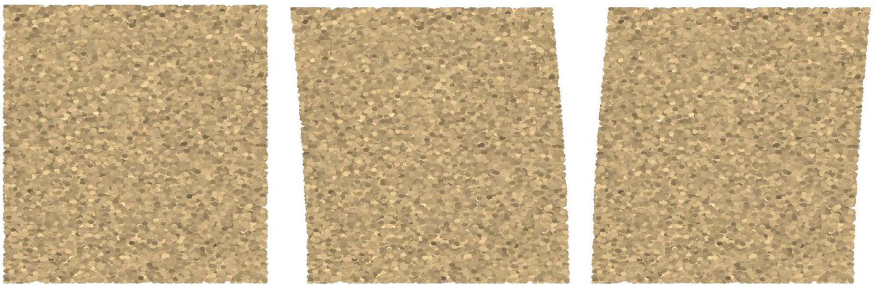

Figure 2. Simulation image of non-uniform shear deformation of sand.

$$\sin\left(\mathrm{MAX}_t \cdot \frac{y}{h} \cdot \frac{\pi}{2}\right) \tag{2}$$

Among them, MAX_t is the maximum deformation of the simulated deformation time history at time t, h is the height of the image, and y is the longitudinal coordinate value of the current particle.

3. Analysis of Influencing Factors

Deformation induces relative movements of soil particles within an image subset, altering textural characteristics. This affects subset matching and localization, leading to increased errors in the computed displacement field. Such errors are further amplified in subsequent strain calculations, making the analysis of strain fields and strain time histories particularly challenging for image-based deformation measurement techniques.

The choice of strain calculation method is critical to the accuracy of strain results. The central difference method is commonly used for strain estimation; however, both theoretical and experimental studies have shown that it is highly sensitive to noise in the displacement field, producing inaccurate and scattered results. In contrast, the local least-squares fitting method yields a more accurate and smoother strain field. This method operates by selecting a region of size $(2M + 1) \times (2M + 1)$ around the measurement point and fitting the displacement data within this region. The strain components at the point are then derived from the coefficients of the fit.

As shown in **Figure 3**, let $u(x,y)$ and $v(x,y)$ represent the displacements in the x- and y-directions at point (x, y), respectively. Applying the fitting form given in Equation (3), coefficient $a_1 = \partial u/\partial x$ corresponds to the normal strain in the x-direction, $a_2 = \partial u/\partial y$ to the shear strain related to the x-direction, $a_4 = \partial v/\partial y$ to the normal strain in the y-direction, and $a_3 = \partial v/\partial x$ to the shear strain related to the y-direction. It is evident that the size of the strain calculation window, *i.e.*, the $(2M + 1) \times (2M + 1)$ region, critically determines the values of the fitting parameters a_1, a_2, a_3 and a_4.

$$\begin{aligned} u(x,y) &= a_0 + a_1 x + a_2 y \\ v(x,y) &= a_3 + a_4 x + a_5 y \end{aligned} \tag{3}$$

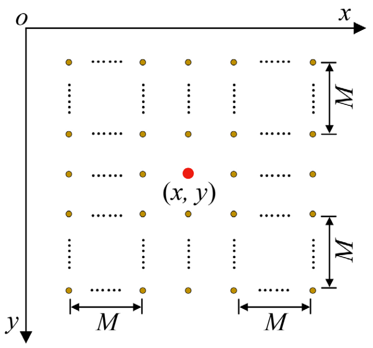

Figure 3. The strain calculation window of measuring point (*x*, *y*).

3.1. Window Size

We first investigated the influence of window size on computational error under uniformly distributed strain. Uniform shear strains of 0.1%, 1%, and 10% were applied to the simulated images. The displacement fields were computed through image deformation analysis. Missing data, erroneous vectors, and noise were then filtered from the obtained displacement fields. Strain was subsequently calculated using different window sizes, and the computational errors are summarized in **Table 1**.

Table 1. Errors of different strain sizes and calculation windows.

Error	Strain	Strain calculation window				
		5 × 5	9 × 9	13 × 13	17 × 17	21 × 21
Average error	0.1%	46.5%	25.8%	22.0%	18.7%	16.0%
	1%	39.6%	25.4%	17.6%	13.2%	9.8%
	10%	4.0%	2.4%	1.5%	1.0%	0.7%
Coefficient of variation	0.1%	0.62	0.45	0.39	0.34	0.30
	1%	0.51	0.31	0.21	0.16	0.12
	10%	0.05	0.03	0.02	0.01	0.01
Maximum error	0.1%	430%	190%	170%	130%	99%
	1%	314%	142%	77%	46%	33%
	10%	31%	15%	9%	5%	3%

The results under uniform strain conditions indicate that: 1) the mean error, coefficient of variation, and maximum error(maximum value of absolute errors) all decrease with increasing window size, demonstrating that larger windows significantly enhance computational accuracy; 2) a small calculation window results in a high coefficient of variation, indicating higher dispersion in the strain field, as smaller windows are insufficient to smooth the noise present in the displacement field; 3) a strong correlation exists between the required window size and the strain magnitude. Smaller strain values are associated with greater relative errors, thus necessitating larger windows for effective filtering and smoothing.

In summary, strain calculation error is subject to the coupling effect between the calculation window size and the strain magnitude. Assuming a mean error of 20% as the acceptable threshold, the minimum window sizes for strains of 0.1%, 1%, and 10% should be no less than 17 × 17, 13 × 13, and 5 × 5, respectively.

For non-homogeneous strain distributions, a sinusoidal function was applied to simulated images to introduce nonlinear shear strain variations from 0% to 10%. The displacement fields were derived using image deformation analysis methods and then smoothed. Strain fields were computed using different computation window sizes, as shown in **Figure 4**. The corresponding mean and maximum errors for each window size are presented in **Figure 5**. **Figure 4** and **Figure 5** reveal that under non-homogeneous strain conditions, when a small computation window is used, the strain field exhibits high variability. In contrast, a larger window reduces variability and yields a smoother strain field. However, an excessively large window leads to significant deviations from the theoretical strain values, particularly an underestimation of the maximum strain. This occurs because a large window covers numerous regions with different strain levels, and the strain computation process averages the values over the entire window. The greater the strain variation within the window, the greater the deviation of the computed result from the true value. These findings highlight the crucial importance of selecting an appropriate computation window size in strain analysis under non-uniform deformation conditions. A well-chosen window size ensures both smoothness of the strain field and accuracy in capturing local variations.

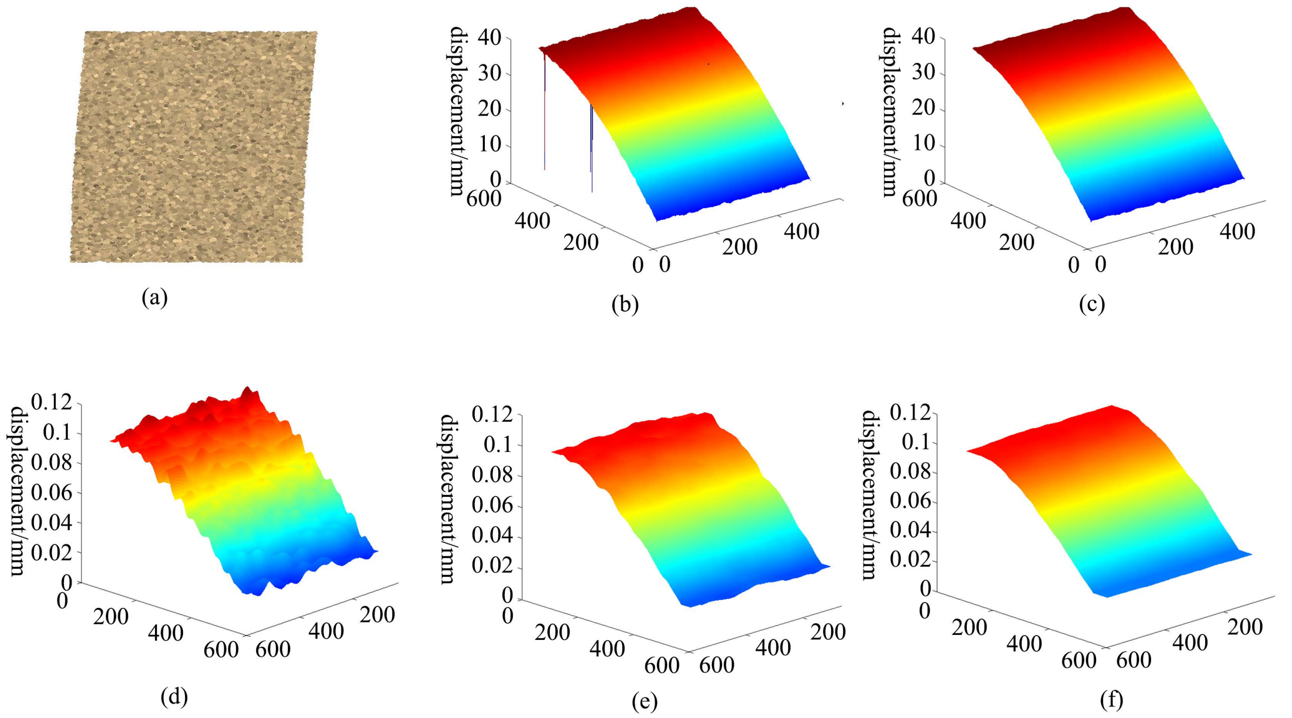

Figure 4. Calculation results of different strain calculation windows. (a) image of sand simulation, (b) original displacement, (c) smoothed displacement, (d) strain by 9 × 9 window, (e) strain by 17 × 17 window, (f) strain by 25 × 25 window.

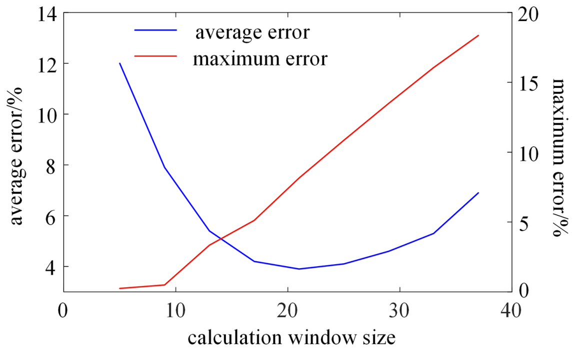

Figure 5. Variation of calculation error of non-uniform strain with window size.

3.2. Image Frame Rate

Accurate measurement of dynamic displacement, acceleration, and strain in soil under cyclic or seismic loading is essential in geotechnical and earthquake engineering research. Recent advances in image-based measurement techniques provide non-contact solutions for tracking soil deformation, offering spatial and temporal resolution that traditional sensors may lack. However, the accuracy of displacement derived from image sequences is influenced by several factors, including image acquisition frame rate, loading frequency, and the signal-to-noise ratio of the imaging system.

In this study, simulated image sequences of an 8 g, 50 Hz sinusoidal excitation were analyzed. The dynamic displacement at a selected point—obtained by applying a 3 × 3 spatial averaging filter around the measurement point to mitigate noise—was measured under various image acquisition frame rates. As shown in **Figure 6** and **Table 2**, the errors in peak displacement values were systematically evaluated for sinusoidal waves with a fixed amplitude (8 g) but varying frequencies and frame rates. These errors are of particular concern as they can be amplified during subsequent calculations of acceleration and strain. Thus, the following thresholds were adopted: a peak displacement error of 10% and peak acceleration and strain errors of 20% were considered acceptable for engineering applications. The results indicate that when the image acquisition frame rate is at least six times the input frequency, displacement can be tracked with high accuracy, with the mean error of the measured peak displacements consistently below 10%. Moreover, the close agreement among the peak displacement values measured at different frame rates demonstrates the robustness of the image-based computational approach.

Table 2. Average peak error of sine wave displacement.

Sine wave frequency/Hz	Image acquisition frame rate/sine wave frequency				
	4	6	10	20	40
10	23%	9.5%	4.9%	0.01%	0.2%
20	9.4%	7.6%	4.7%	0.06%	0.02%
50	19.1%	4.9%	4.4%	0.04%	0.03%
100	19.6%	9.5%	5.1%	2.1%	0.6%

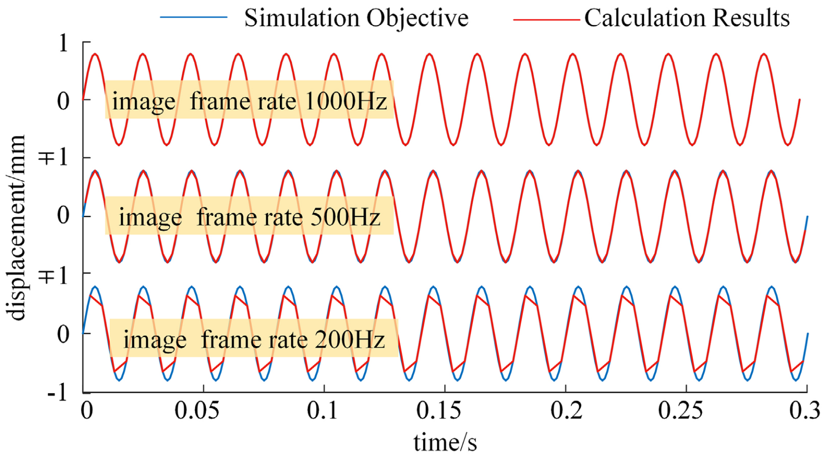

Figure 6. The displacement time history of 8 g 50 Hz sine wave.

Subsequently, acceleration time histories were derived by applying a low-pass filter and double differentiation to the displacement data. The resulting acceleration measurements under different frame rates are presented in **Figure 7**. **Table 3** summarizes the errors in the calculated peak acceleration across different input frequencies and frame rates. The results confirm that when the frame rate is at least six times the loading frequency, the acceleration time history is accurately captured, with mean peak errors remaining below 20%.

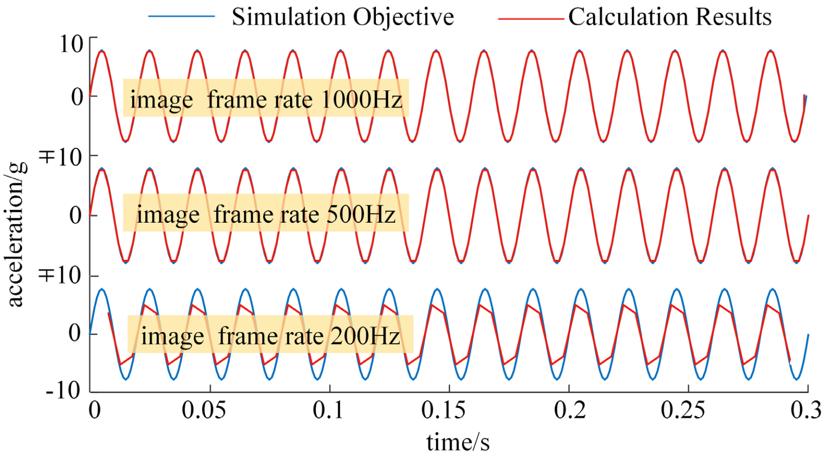

Figure 7. Acceleration time history of a sine wave of 8 g 50 Hz.

Table 3. Average peak error of sine wave acceleration.

Sine wave frequency/Hz	Image acquisition frame rate/sine wave frequency				
	4	6	10	20	40
10	19.1%	16.9%	8%	0.7%	0.1%
20	21.6%	16.3%	8.1%	1.7%	0.5%
50	34.4%	11.7%	7.6%	2.3%	0.7%
100	30.1%	16.9%	7.3%	4.9%	2.5%

To further evaluate the reliability of the method, simulated image sequences of three types of seismic waves were generated and analyzed at a fixed image acquisition frame rate of 100 Hz. For each wave, displacement time histories at three arbitrarily selected points were compared, as shown in **Figure 8**. The excellent agreement among these results underscores the exceptional stability of the computational method. Additional analyses were conducted using the Tangshan wave at varying frame rates—100 Hz, 10 Hz, 4 Hz, and 2 Hz (**Figure 9**). The results show a clear trend: measurement error decreases as frame rate increases. As summarized in **Table 4**, when the frame rate is ≥4 Hz, the average errors (arithmetic mean of absolute errors) in peak displacement are ≤5.5%, ≤7.0%, and ≤7.4% for the three seismic waves, respectively, confirming high accuracy under these conditions.

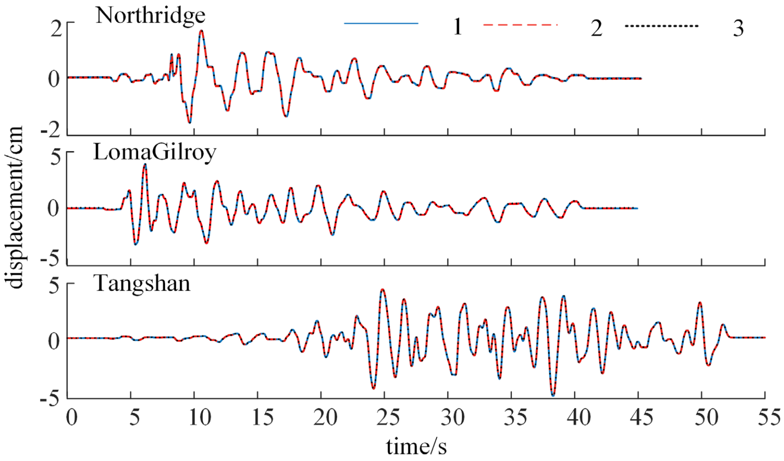

Figure 8. Comparison of displacement time history of 3 points selected from three seismic wave calculation results.

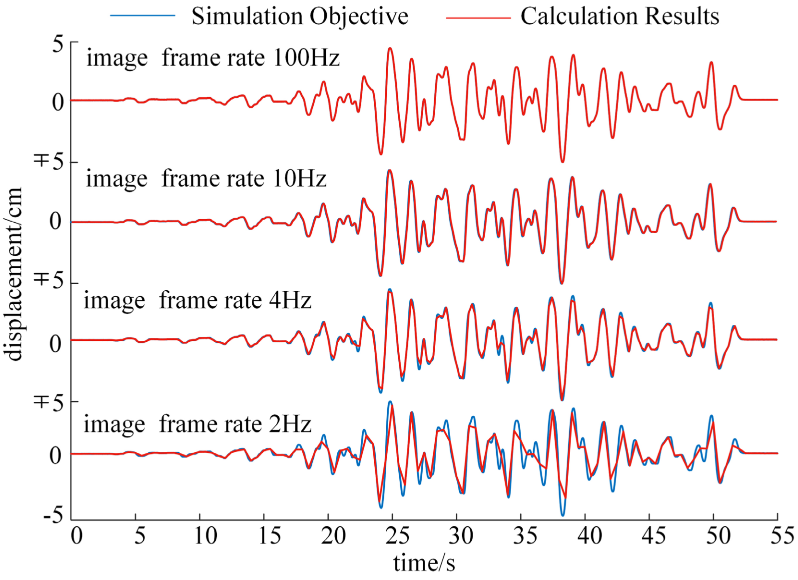

Figure 9. Comparison of seismic wave displacement time history.

Table 4. Average peak error of seismic wave displacement.

Simulated wave	Image acquisition frame rate/Hz				
	2	4	6	10	20
Northridge	18.4%	5.5%	3.5%	1.6%	0.8%
LomaGilroy	15.2%	7.0%	5.4%	5.1%	6.1%
Tangshan	21.3%	7.4%	1.2%	0.5%	0.2%

Acceleration time histories under seismic loading were obtained by processing the displacement records via low-pass filtering and double differentiation. For the Tangshan wave, comparisons at frame rates of 100 Hz, 10 Hz, 4 Hz, and 2 Hz (**Figure 10**) reveal that accurately reproducing acceleration requires higher frame rates than displacement. Both the peak values and frequency content of the calculated acceleration degrade noticeably as the frame rate decreases. It is also noted that excessively high frame rates (e.g., 100 Hz in **Figure 10**) can introduce high-frequency glitches, indicating that beyond a certain threshold, further increases in frame rate may not improve accuracy and can even introduce noise. **Table 5** presents the mean peak acceleration errors for the three seismic waves at frame rates of 20 Hz, 10 Hz, 6 Hz, 4 Hz, and 2 Hz. The results demonstrate that higher-frequency ground motions require higher frame rates to maintain precision. The mean peak acceleration errors are ≤17.7%, ≤8.9%, and ≤10.5% for frame rates ≥ 20 Hz, ≥10 Hz, and ≥6 Hz, respectively—all within the acceptable limit of 20%, confirming that image-based measurements are suitable for dynamic soil response analysis under seismic conditions.

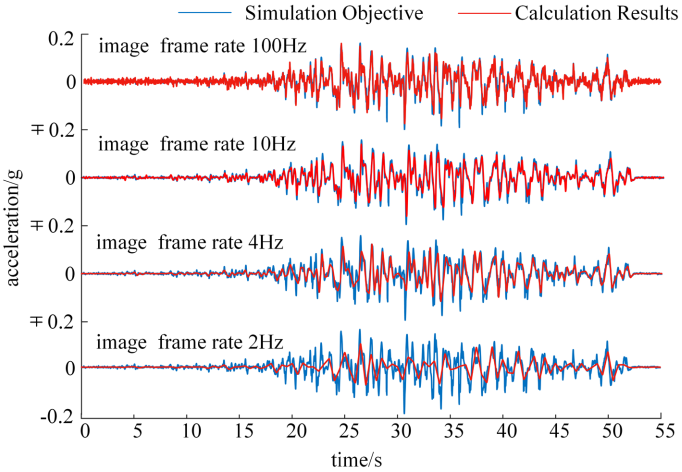

Figure 10. Comparison of seismic wave acceleration time history.

Table 5. Average peak error of seismic wave acceleration.

Simulated wave	Image acquisition frame rate/Hz				
	2	4	6	10	20
Northridge	75.4%	53.9%	42.6%	29.7%	17.7%
Loma Gilroy	61.3%	34.7%	30.1%	8.9%	4.9%
Tangshan	53.7%	26.5%	10.5%	9.9%	6.4%

3.3. Deformation Magnitude

Simulated image sequences were subjected to sinusoidal loading with maximum deformation amplitudes of 0.01 mm, 0.1 mm, 1 mm, and 10 mm to simulate one-dimensional translational motion. The displacement fields were computed using two image deformation analysis methods: RG-DIC and PIVlab (a particle image velocimetry toolbox based on MATLAB). After filtering out missing data, anomalous vectors, and noise from the displacement fields, a point was randomly selected for displacement time history analysis. The resulting errors are shown in **Figure 11**, which demonstrates that under one-dimensional translation conditions, the analysis errors of both RG-DIC and PIVlab decrease with increasing vibration amplitude. When the vibration amplitude is ≥0.1 mm, the errors from both methods are negligible and nearly identical. However, when the amplitude is reduced to ≤0.01 mm, the error for RG-DIC can reach 10%, whereas PIVlab exhibits a superior performance with an error of only approximately 3%.

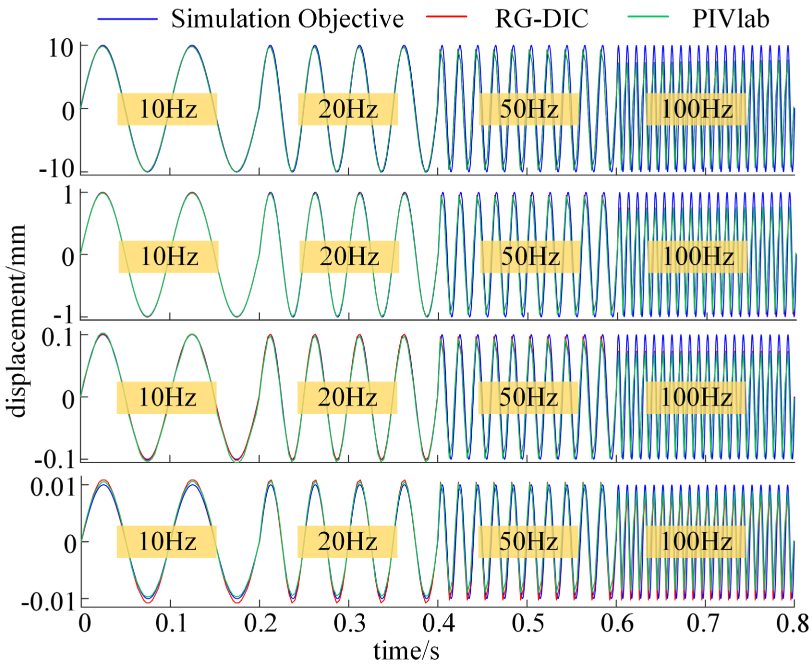

Figure 11. Comparison of the analysis results of different amplitude sine waves.

Using the same approach, the simulated images were subjected to EL Centro seismic loading with maximum amplitudes of 0.01 mm, 0.05 mm, 0.5 mm, 5 mm, and 50 mm. A comparison between the simulated and computed displacement time histories is presented in **Figure 12**. The results indicate that RG-DIC yields closer agreement with the simulated input than PIVlab. The analysis error of both methods decreases with increasing displacement amplitude. However, at the amplitude of 50 mm, the results from PIVlab exhibit severe deviation from the prescribed values. This is primarily due to the propagation and accumulation of outliers during the cumulative displacement calculation in PIVlab.

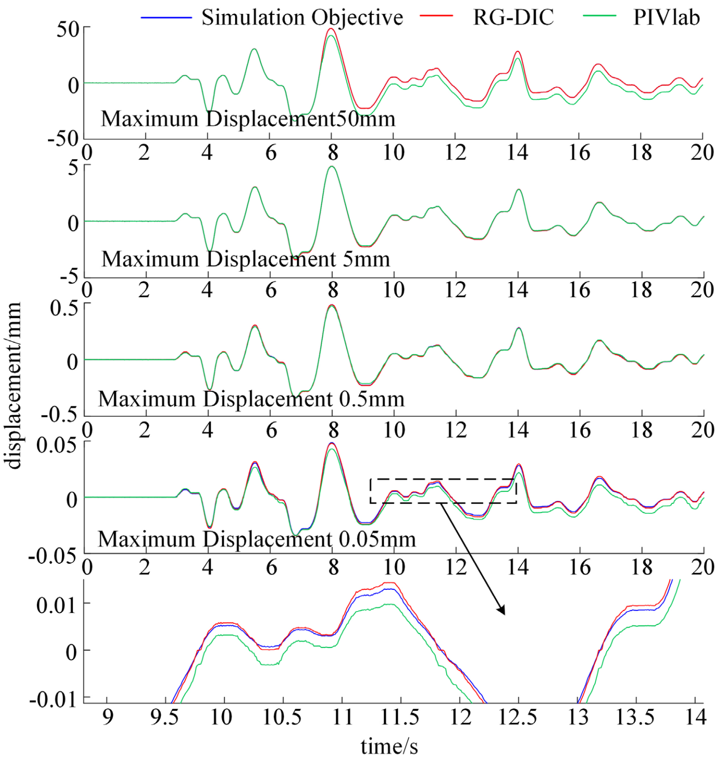

Figure 12. Comparison of displacement analysis results of EL Centro waves with different amplitudes.

Acceleration time histories were obtained by applying a low-pass filter and double differentiation to the displacement data, as shown in **Figure 13**. In contrast to the displacement time histories, the acceleration profiles are largely unaffected by outliers from the cumulative displacement process. As the vibration amplitude decreases, the error in the computed acceleration increases, accompanied by high-frequency fluctuations or "glitches". For instance, at a low acceleration level of 0.02 m/s^2, the acceleration time history from PIVlab shows significant oscillation (**Figure 13**). This occurs because the displacement time history obtained by PIVlab is noisier than that from RG-DIC, and these minor discrepancies are greatly amplified during differentiation. While RG-DIC accurately recovers the prescribed seismic motion, PIVlab only produces consistent results when the maximum displacement reaches ≥5 mm.

Under large deformation conditions, PIVlab obtains the instantaneous displacement field through particle matching between adjacent image frames, and then derives the velocity field by performing differentiation on the displacement field. This process carries significant risk of error accumulation: in large deformation scenarios, when the pixel displacement between adjacent frames exceeds the preset search window range of PIVlab, particle matching is prone to mismatching, which introduces local errors into the displacement field; subsequent displacement calculations rely on this displacement field, and the local displacement errors are continuously amplified during the differentiation process, eventually leading to obvious deviations.

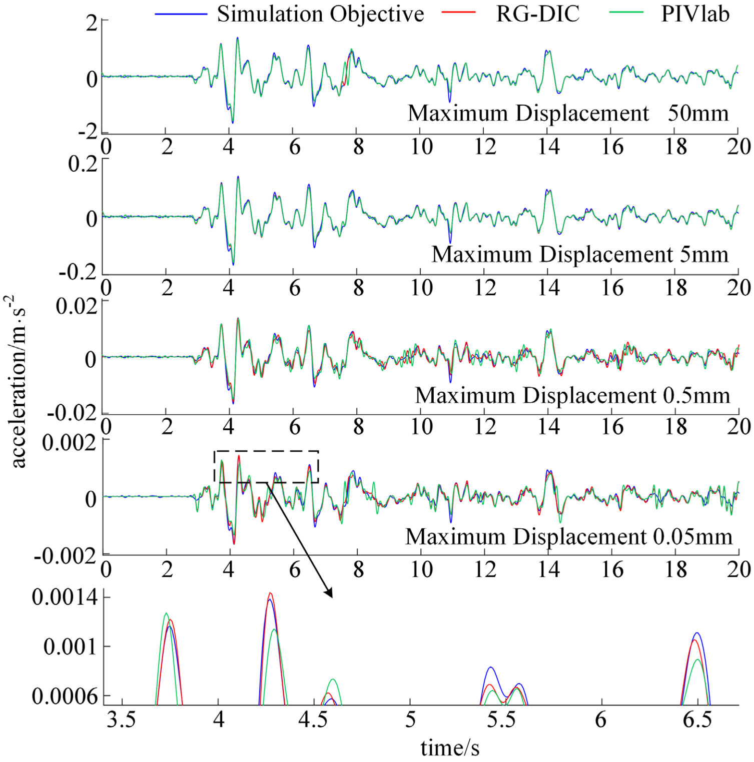

Figure 13. Comparison of acceleration analysis results of EL Centro waves with different amplitudes.

4. Conclusions

This study employed synthetic images of digitally generated sand particles to evaluate the measurement accuracy of image deformation analysis techniques in tracking soil dynamic response. The investigation focused on the effects of different interrogation window sizes and magnitudes of deformation, as well as the influence of the algorithms employed and external disturbances during the dynamic time-history computation. The main conclusions are summarized as follows:

1) Image-based deformation measurement techniques are capable of accurately retrieving dynamic time histories (e.g., displacement, acceleration, and strain) at any point on the observed surface. The results show high consistency with the preset dynamic deformation time histories. This approach offers a crucial technique for enhancing the understanding of site-specific seismic response and the failure mechanisms of geotechnical structures, as well as for evaluating the reliability of conventional embedded point-based sensing techniques.

2) Under constant strain conditions, an increase in either the strain computation window size or the preset strain magnitude leads to a reduction in strain calculation errors. In contrast, under non-uniform strain conditions, an excessively large computation window may cause significant distortion in the analysis results.

3) To measure dynamic soil deformation under sinusoidal loading, the image acquisition frame rate should be at least six times the loading frequency. This criterion ensures that the mean peak errors for displacement and acceleration remain

within 10% and 20%, respectively. For seismic wave loading, the required frame rates are ≥20 Hz, ≥10 Hz, and ≥6 Hz for the Northridge, Loma Gilroy, and Tangshan waves, respectively. For cases involving small deformations, the acceleration time history derived using PIVlab exhibits significant oscillations, which arise from the amplification of minor errors in the displacement data during numerical differentiation.

4) It should be noted that this study verified the accuracy based on simulated images. However, in real physical experiments, several factors may affect the practical application effect of the method: camera noise may undermine the stability of texture matching, lens distortion tends to introduce systematic deviations, and out-of-plane motion may lead to displacement misjudgment and image blurring. In future research, the robustness and practicality of the method in complex experimental scenarios can be further improved by integrating modules for image denoising, pre-calibration of lens distortion, and out-of-plane motion compensation, thereby providing more reliable technical support for high-precision displacement measurement in the engineering field.

Acknowledgements

The authors are grateful for the financial support of the major science and technology support plan of Hebei Province (252J5401D).

Conflicts of Interest

The authors declare no conflicts of interest regarding the publication of this paper.

References

[1] Bowman, A.J. and Haigh, S.K. (2019) Subsurface Deformation Mechanisms Beneath a Flexible Pavement Using Image Correlation. *Géotechnique*, **69**, 627-637. https://doi.org/10.1680/jgeot.18.p.092

[2] Bruck, H.A., McNeill, S.R., Sutton, M.A. and Peters, W.H. (1989) Digital Image Correlation Using Newton-Raphson Method of Partial Differential Correction. *Experimental Mechanics*, **29**, 261-267. https://doi.org/10.1007/bf02321405

[3] Chen, Z., Li, K., Omidvar, M. and Iskander, M. (2017) Guidelines for DIC in Geotechnical Engineering Research. *International Journal of Physical Modelling in Geotechnics*, **17**, 3-22. https://doi.org/10.1680/jphmg.15.00040

[4] White, D.J., Take, W.A. and Bolton, M.D. (2003) Soil Deformation Measurement Using Particle Image Velocimetry (PIV) and Photogrammetry. *Géotechnique*, **53**, 619-631. https://doi.org/10.1680/geot.2003.53.7.619

[5] Chen, J., Zhang, X. and Zhan, N. (2011) Extended Digital Image Correlation Method for Micro-Region Deformation Measurement. *Science China Technological Sciences*, **54**, 1355-1361. https://doi.org/10.1007/s11431-011-4404-2

[6] Pan, B., Qian, K., Xie, H. and Asundi, A. (2009) Two-Dimensional Digital Image Correlation for In-Plane Displacement and Strain Measurement: A Review. *Measurement Science and Technology*, **20**, Article ID: 062001. https://doi.org/10.1088/0957-0233/20/6/062001

[7] Teng, Y., Stanier, S.A. and Gourvenec, S.M. (2017) Synchronised Multi-Scale Image

Analysis of Soil Deformations. *International Journal of Physical Modelling in Geotechnics*, **17**, 53-71. https://doi.org/10.1680/jphmg.15.00058

[8] Sadek, S., Iskander, M.G. and Liu, J. (2003) Accuracy of Digital Image Correlation for Measuring Deformations in Transparent Media. *Journal of Computing in Civil Engineering*, **17**, 88-96. https://doi.org/10.1061/(asce)0887-3801(2003)17:2(88)

[9] Bessette, C., Brito, L., Dashti, S., Liel, A.B. and Wham, B.P. (2024) Development of Dynamic Centrifuge Models for Measurement and Visualization of Deformation Mechanisms in Liquefiable Soils. *Soil Dynamics and Earthquake Engineering*, **181**, Article ID: 108651. https://doi.org/10.1016/j.soildyn.2024.108651

[10] Malvick, E.J., Kutter, B.L. and Boulanger, R.W. (2008) Postshaking Shear Strain Localization in a Centrifuge Model of a Saturated Sand Slope. *Journal of Geotechnical and Geoenvironmental Engineering*, **134**, 164-174. https://doi.org/10.1061/(asce)1090-0241(2008)134:2(164)

[11] Stanier, S.A., Blaber, J., Take, W.A. and White, D.J. (2016) Improved Image-Based Deformation Measurement for Geotechnical Applications. *Canadian Geotechnical Journal*, **53**, 727-739. https://doi.org/10.1139/cgj-2015-0253

[12] Zappa, E., Mazzoleni, P. and Matinmanesh, A. (2014) Uncertainty Assessment of Digital Image Correlation Method in Dynamic Applications. *Optics and Lasers in Engineering*, **56**, 140-151. https://doi.org/10.1016/j.optlaseng.2013.12.016

[13] Zhang, G., Mou, T.P. and Zhang, J.M. (2007) Displacement Measurement Using Image Analysis in Centrifuge Modeling of Slopes. *Chinese Journal of Geotechnical Engineering*, No. 1, 94-97.

[14] Gao, G., Huang, S., Xia, K. and Li, Z. (2014) Application of Digital Image Correlation (DIC) in Dynamic Notched Semi-Circular Bend (NSCB) Tests. *Experimental Mechanics*, **55**, 95-104. https://doi.org/10.1007/s11340-014-9863-5

[15] Siebert, T. (2007) High-speed Digital Image Correlation: Error Estimations and Applications. *Optical Engineering*, **46**, Article ID: 051004. https://doi.org/10.1117/1.2741217

[16] Bornert, M., Brémand, F., Doumalin, P., *et al.* (2009) Addendum to: Assessment of Digital Image Correlation Measurement Errors: Methodology and Results. *Experimental Mechanics*, **49**, 353-370.

[17] Pan, B., Xie, H., Wang, Z., Qian, K. and Wang, Z. (2008) Study on Subset Size Selection in Digital Image Correlation for Speckle Patterns. *Optics Express*, **16**, 7037-7048. https://doi.org/10.1364/oe.16.007037

[18] Sun, Y.F. and Pang, J.H.J. (2007) Study of Optimal Subset Size in Digital Image Correlation of Speckle Pattern Images. *Optics and Lasers in Engineering*, **45**, 967-974. https://doi.org/10.1016/j.optlaseng.2007.01.012

[19] Hua, T., Xie, H.M., Wang, S., *et al.* (2011) Evaluation of the Quality of a Speckle Pattern in the Digital Image Correlation Method by Mean Subset Fluctuation, *Optics & Laser Technology*, **43**, 9-13.

[20] Wang, Y.Z., Duan, X.F., Chen, S., *et al.* (2024) An Approach of Synthetic Sand Deformation Images Based on Grain Features and Prescribed Traces and Application. *Chinese Journal of Geotechnical Engineering*, **46**, 1047-1056. https://link.cnki.net/urlid/32.1124.TU.20231209.2106.002

[21] Stanier, S.A. and White, D.J. (2013) Improved Image-Based Deformation Measurement in the Centrifuge Environment. *Geotechnical Testing Journal*, **36**, 915-928. https://doi.org/10.1520/gtj20130044